

Astro-photometric study of M37 with *Gaia* and wide-field *ugi*-imaging

M. Griggio,^{1,2★} L. R. Bedin^{1b},² R. Raddi^{1b},³ N. Reindl,⁴ L. Tomasella^{1b},² M. Scalco,^{1,2} M. Salaris,^{5,6} S. Cassisi,⁶ P. Ochner,^{2,7} S. Ciroi,⁷ P. Rosati,¹ D. Nardiello^{1b},² J. Anderson,⁸ M. Libralato^{1b},⁹ A. Bellini,⁸ A. Vallenari,² L. Spina² and M. Pedani¹⁰

¹Dipartimento di Fisica, Università di Ferrara, Via Giuseppe Saragat 1, I-44122 Ferrara, Italy

²INAF – Osservatorio Astronomico di Padova, Vicolo dell’Osservatorio 5, I-35122 Padova, Italy

³Universitat Politècnica de Catalunya, Departament de Física, c/ Esteve Terrades 5, E-08860 Castelldefels, Spain

⁴Institut für Physik und Astronomie, Universität Potsdam, Karl-Liebknecht-Straße 24/25, D-14476 Potsdam, Germany

⁵Astrophysics Research Institute, Liverpool John Moores University, 146 Brownlow Hill, Liverpool L3 5RF, UK

⁶INAF – Osservatorio Astronomico di Abruzzo, Via M. Maggini, I-64100 Teramo, Italy

⁷Department of Physics and Astronomy, University of Padova, Via F. Marzolo 8, I-35131 Padova, Italy

⁸Space Telescope Science Institute, 3700 San Martin Drive, Baltimore, MD 21218, USA

⁹AURA for the European Space Agency (ESA), Space Telescope Science Institute, 3700 San Martin Drive, Baltimore, MD 21218, USA

¹⁰Fundación Galileo Galilei – INAF, Rambla José Ana Fernández Pérez 7, E-38712 Breña Baja (TF), Spain

Accepted 2022 July 6. Received 2022 July 5; in original form 2022 June 15

ABSTRACT

We present an astrometric and photometric wide-field study of the Galactic open star cluster M37 (NGC 2099). The studied field was observed with ground-based images covering a region of about four square degrees in the *Sloan*-like filters *ugi*. We exploited the *Gaia* catalogue to calibrate the geometric distortion of the large field mosaics, developing software routines that can be also applied to other wide-field instruments. The data are used to identify the hottest white dwarf (WD) member candidates of M37. Thanks to the *Gaia* EDR3 exquisite astrometry we identified seven such WD candidates, one of which, besides being a high-probability astrometric member, is the putative central star of a planetary nebula. To our knowledge, this is a unique object in an open cluster, and we have obtained follow-up low-resolution spectra that are used for a qualitative characterization of this young WD. Finally, we publicly release a three-colour atlas and a catalogue of the sources in the field of view, which represents a complement of existing material.

Key words: catalogues – white dwarfs – open clusters and associations: individual: M37 (NGC 2099).

1 INTRODUCTION

The vast majority of low- to intermediate-mass stars in the Galaxy end their lives as white dwarfs (WDs). Their nature of compact objects has served as an important test case for many areas of fundamental physics and stellar evolution theories. WDs in open clusters (OCs) represent a unique opportunity to study these objects in well characterized environments, as OCs usually have very well-determined properties such as age, distance, metallicity, and reddening.

M37, also known as NGC 2099, is a rich (with an estimated total mass of $\sim 1500 M_{\odot}$ by Piskunov et al. 2008), intermediate-age OC, with an angular size of about 1 deg (Griggio & Bedin 2022). As revealed by Cordoni et al. (2018), this cluster exhibits an extended Main-Sequence (MS) Turn-Off, thus its precise age is still under debate; Mermilliod et al. (1996) gives an age of about 400–500 Myr, compatible with the more recent estimate by Cordoni et al. (2018) that gives an age of 550 Myr. M37 is located in the Auriga constellation, at a distance of about 1.4 kpc (Kharchenko et al. 2005; Griggio & Bedin 2022). It has been the object of several photometric studies (e.g. Kalirai et al. 2001) as well as spectroscopic investigations (e.g.

Pancino et al. 2010). Both photometric and spectroscopic analyses mostly agree on the metallicity of this cluster, which is around solar ($[Fe/H] = 0.02 - 0.08$; Heiter et al. 2014; Netopil et al. 2016; Casamiquela et al. 2019), and give a reddening estimate in the range 0.2–0.3 (e.g. Sarajedini et al. 2004; Kang et al. 2007). M37 has been long known to host quite a large population of WD candidates, consisting of ~ 50 stars that were identified via deep *B*- and *V*-band photometry down to $V = 23.5$ mag (Kalirai et al. 2001) and were characterized through optical spectroscopy (Kalirai et al. 2005). More recently, spectroscopic follow-up have confirmed, rejected, or identified new cluster members (Cummings et al. 2015), including a very massive $\sim 1.28 M_{\odot}$ object (Cummings et al. 2016). The WD census of this OC is not yet complete due to several reasons, like source crowding, dispersal of cluster members, unresolved binarity with MS companions; current estimates outnumber the WD candidates by a factor of 2–4 (Kalirai et al. 2001; Richer et al. 2021). Despite their faintness, 10–15 confirmed WD members have been extensively studied for the characterization of the initial-to-final-mass relation (IFMR), leading to an increasingly improved understanding of mass-loss for low- to intermediate-mass stars (Ferrario et al. 2005; Catalán et al. 2008; Salaris et al. 2009; Cummings et al. 2018).

★ E-mail: massimo.griggio@inaf.it

Table 1. Data set used in this work. All the observations were carried out in 2020 November.

Filter	# of exp. $\times t_{\text{exp}}$	Airmass (arcsec) (best-worst)	Seeing (arcsec) (best-worst)
<i>i</i>	66×240 s	1.03–1.72	1.51–3.22
	22×10 s	1.03–1.73	1.47–3.04
<i>g</i>	66×240 s	1.03–1.84	1.53–3.25
	22×10 s	1.03–1.85	1.52–3.05
<i>u</i>	66×240 s	1.04–1.97	1.55–2.40
	23×10 s	1.04–1.98	1.53–2.63

In this paper, we employ observations of M37 collected at the Asiago Schmidt telescope¹ in the *Sloan*-like *ugi* filters to develop and test a procedure to calibrate the geometric distortion of the instrument, exploiting the *Gaia* Early Data Release 3 (EDR3; *Gaia* Collaboration 2021) absolute reference system, which will be applied also to other wide-field imager mosaics.

By using the method of astrometric cluster membership presented in Griggio & Bedin (2022), we have identified seven new WD member candidates that are currently at the hot end of the WD cooling sequence, which has so far been overlooked by previous searches. These new candidates include the likely central star of a planetary nebula, for which we have also obtained two sets of follow-up spectra. We analyse their physical properties and further discuss their cluster membership.

In Sections 2 and 3 we describe the observations and the data reduction routines. In Sections 4 and 5 we use the membership probability and the astrometric parameters to select cluster members, and we show the colour–magnitude diagrams in the *ugi* filters. The newly identified WD member candidates and their spectral energy distribution analysis are presented in Section 6. Section 7 describes the catalogue that we publicly release.

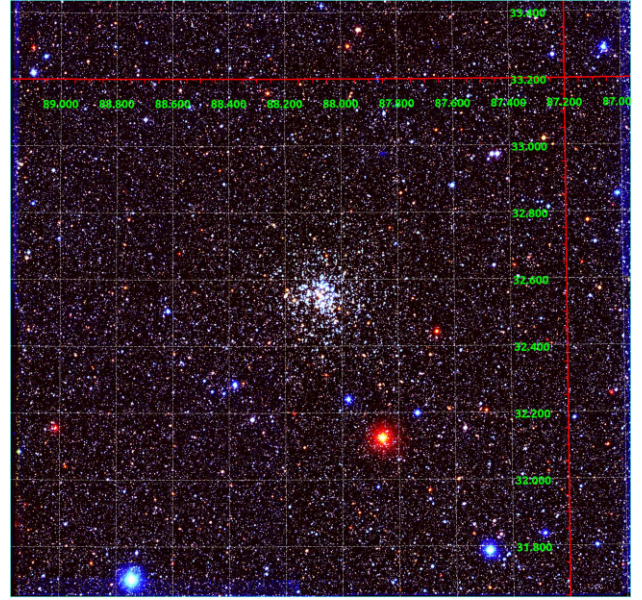
2 DATA SET

The data were collected with the Schmidt 67/92 cm telescope in Asiago (Italy) between 2020 November 8 and 21. The telescope is equipped with a KAF-16803 CCD, with an active area of 4096×4096 pixels and a field of view (FOV) of 59×59 arcmin², that corresponds to a ~ 0.87 arcsec px^{−1} scale. We collected a mosaic of about 2×2 deg², with a ~ 13 arcmin overlap. All the tiles of the mosaic were dithered, and images collected in three filters, *u*-, *g*-, *i*-*Sloan*, for a total of 198 images (some of which were later discarded due to poor image quality) each with a 240 s exposure time. In addition, we collected a set of images with a 10 s exposure time to have a better estimation of the flux of very bright sources that are saturated in the 240 s data. Table 1 summarizes the observation logs.

The mosaic covers an area centred on M37. A stacked image in three-colour version is shown in Fig. 1; a description on how the stack was produced will be given in Section 3.4.

3 DATA REDUCTION

The data have been corrected via standard calibrations (bias, dark, linearity, and flat-field). In addition, we accounted for the effects of



frame (projected on to the tangent plane of each exposure), and then we computed for each star in each catalogue the residuals between the transformed positions and those given by *Gaia*. We divided the residuals from all the catalogues in bins of 200×200 pixels, and for each bin we calculated the mean residual in x and y . The distortion correction routine uses this map of residuals to correct the position of each star via a bi-linear interpolation between the four nearest grid points. In Fig. 2 we show an example of distortion map before and after the correction, left and right, respectively. In the figure we see the CCD divided into 21×21 bins, where the arrows represent the mean residual of each bin. Before applying the correction, in particular near the edges of the detector, the distortion goes up to 0.15 pixels, while after the correction have been applied the distortion is less than 0.05 pixels (about 40 mas).

3.3 The master frame

The next step is to put all our images into a common reference frame. This allows us to measure the same star in different exposures simultaneously, thus increasing the signal for fainter sources. The coordinate system on the CCD lies on the plane tangent to the celestial sphere at the central point of the FOV. Since our images have large dithers, each of the 2×2 fields lies in a significantly different tangent plane, as discussed also in Libralato et al. (2015) for a different detector.

In order to derive the coordinate transformations to put every image in the same tangent plane, we took advantage of the *Gaia* absolute reference frame. We started by cross-referencing the stars in our preliminary photometry catalogues with the *Gaia* EDR3, after correcting their positions for geometric distortions of the field. The *Gaia* coordinates were corrected for proper motions to be reported at the epoch of the observations, and then projected on to the tangent plane of each exposure using the procedure described in Bedin & Fontanive (2018). This allowed us to derive (for each frame) a global six-parameter transformation from the (X, Y) reference system of the CCD to the meta-coordinate system (ξ, η) of its tangent plane.

We then applied the inverse transformation to project back on the celestial sphere our positions, to have all our preliminary catalogues in spherical coordinates (α, δ) . We then arbitrarily chose a point (α_0, δ_0) (the same for all the exposures) to project down again all the catalogues on to a common reference system (that now lies in the same tangent plane for every image): in particular we projected all the catalogues on the tangent plane of the image SC132969 (archival name), and then applied the inverse transformation from the (ξ, η) coordinate system of the tangent plane to the (X, Y) system of the chosen catalogue. After these steps we have all the catalogues lying in the same plane, in physical pixel coordinates (X, Y) , with a mean pixel scale of 868 mas px^{-1} . For the sake of conciseness, in the following we will call ‘preliminary catalogues’ the catalogues after the transformations to get them on to the same coordinate system.

To define the master frame we downloaded a portion of the *Gaia* EDR3 catalogue centred on M37 with a radius of 1.5 deg, we reported the positions of its stars to the observed epoch, we projected it down on the same tangent plane chosen in the previous step and we converted the meta-coordinates to pixel-coordinates by dividing by the pixel scale. For each filter (u, g, i) we compiled an average catalogue combining all the single preliminary catalogues and produced a list of the sources found in at least eight images, giving for each source the 3σ -clipped averaged position and magnitude.

These averaged positions and magnitudes are then cross-referenced with the *Gaia* catalogue to obtain a final list of objects with

Gaia positions and *ugi*-magnitudes. This list is then used as master frame: we compute the transformations between each preliminary catalogue to this reference system, which are then used as input in the next step.

3.4 Second-pass photometry

The second-pass photometry is performed by the software KS2 (an evolution of the code presented in Anderson et al. 2008a) originally developed for *HST* images, modified to suit the Schmidt sensor and data taken with large dither patterns. Below we give a brief overview of the KS2 software, which is described in detail by Bellini et al. (2017a) and Nardiello et al. (2018) (see also Scalco et al. 2021 for a more recent application).

The inputs of the KS2 routine are: the images, the PSFs, and the transformations derived from the preliminary photometry to find and measure the sources in all the exposures simultaneously. The star finding process goes through different iterations, moving progressively from the brightest to the faintest sources. The software takes as input also a list of bright stars from the preliminary photometry and construct weighted masks around them, which help us to avoid PSF-related artefacts. In each iteration the program finds and measures the stars which fit the conditions specified for that iteration, and then subtracts them and proceeds with the next iteration.

KS2 measures, in each image, the flux and position of the source using the appropriate local PSF. The star position and flux is determined by fitting the PSF to its 5×5 central pixels as in the preliminary photometry, but it computes the final position and flux as an average between all the images, with the local sky value computed from the surrounding pixels.

Saturated stars are not measured by KS2; their position and fluxes are recovered by the preliminary photometry and supplemented in the output. To properly measure the stars that were saturated in the 240 s exposures we used the 10 s images. We performed a second-pass photometry on the short exposures separately, with the zero-point registered on the long exposures, and we cross-referenced the sources in the long and short catalogues. We then replaced the magnitudes of the saturated stars in the 240 s catalogue with those measured on the 10 s frames.

The major upgrade in the code is devoted to perform the projections illustrated in Section 3.3 on the images, to make the code suited to wide-field images taken with large dither patterns. The upgraded code takes as input a set of additional files that are needed to perform the transformations between the local and the master frames. The additional files are:

- (i) one file per image containing the coefficients for the six parameters of the most general linear transformation from the local (X, Y) to the (ξ, η) frame of the tangent plane;
- (ii) one file per image containing the tangent point to each frame used for the projection on spherical coordinates;
- (iii) one file that contains the (α_0, δ_0) point needed to project all the frames on to the same tangent plane;
- (iv) one file that contains the parameters to transform the projected positions on the (X, Y) frame of the chosen image.

The KS2 software also outputs an image stack per filter that can be combined for display (as in Fig. 1), although they are not suitable for extracting photometry (details on how the stack is produced are given in Anderson et al. 2008b). As part of this work, we also made publicly available these atlases of the astronomical scene in the three bands *ugi*.

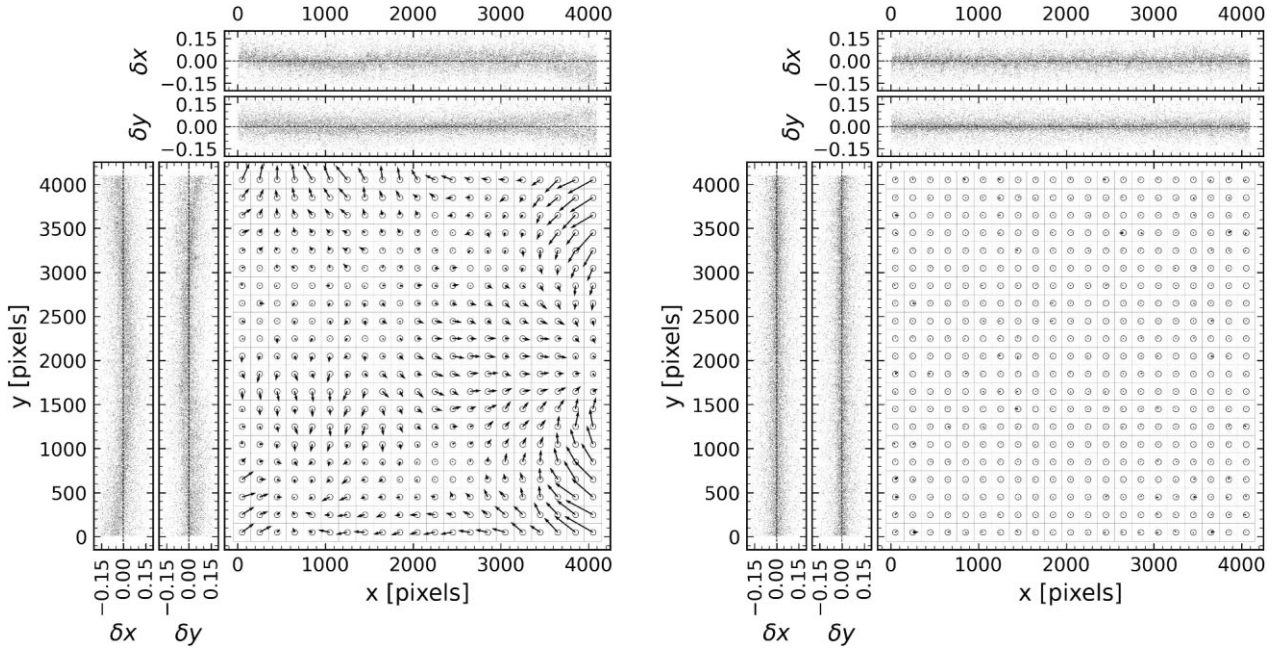


Figure 2. Distortion map for image SC132788 before (left-hand panel) and after (right-hand panel) the distortion correction routine. The central panels represent the CCD coordinate system, with the arrows showing the magnitude and direction of the distortion on each point, corresponding to a 200×200 pixels box. The arrows have been multiplied by a factor 2500 for visualization purposes. On the top and left-hand panels we show a projection on the axes of the x and y components of the distortion.

3.5 Input–output corrections

In extracting photometry for faint stars, the flux is systematically overestimated when the central pixel of a star coincides with a local maximum of the background noise. This is a well-known effect (sometimes referred to as ‘stellar migration’) that needs to be corrected for (see Bedin et al. 2009 for details). In order to assess the systematic errors, we performed an artificial-star (AS) test using the same procedure described in Anderson et al. (2008a). For each AS we chose a random position and u magnitude; the $g - i$ colour is then chosen such that the star falls on the MS ridge-line (drawn by eye). The AS is added in each exposure at the specified position, in the form of an appropriately scaled PSF with Poisson noise. The software routines then operate blindly, finding and measuring all the stars. Examining the output we can determine the accuracy at each magnitude in recovering the AS. Fig. 3 (top panel) shows the difference between the inserted and recovered magnitudes for ASs in the g filter, as function of the instrumental magnitude.

To account for these errors, we derived a correction in the following way: we started dividing the ASs in bins of 0.5 magnitudes. We sigma-clipped each bin (at 2σ) around its median to remove outliers, and calculated the median as an estimator of the residual for that bin. We then interpolated the points with a quadratic spline as a function of the magnitude. We used this relation $m_{\text{IN}} - m_{\text{OUT}}$ versus m to correct the effects of the stellar migration on the magnitudes of the stars in our catalogue. In Fig. 3 (bottom panel) we show the result of this procedure.

3.6 Photometric calibration

Our instrumental magnitudes have been transformed into the Isaac Newton Telescope (INT) Galactic Plane Survey (IGAPS; Monguió et al. 2020) photometric system that merges the INT Photometric

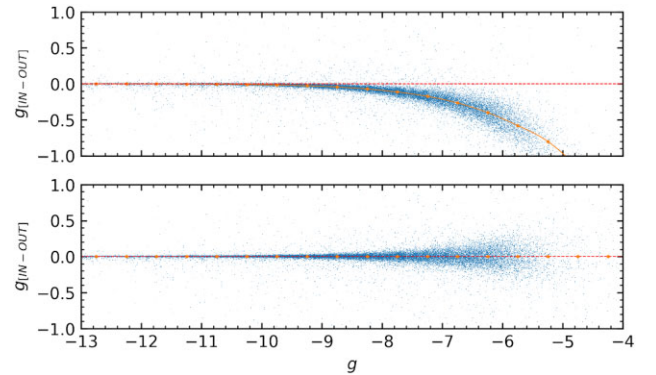


Figure 3. Correction of stellar migration for g -filter magnitudes. Top panel: difference between the inserted and the recovered magnitude. Orange dots are the mean residuals for each magnitude bin. The orange line is the interpolating quadratic spline. The dashed line indicates the null difference. Bottom panel: residuals after the correction. Orange dots are the mean residual for each magnitude bin. The dashed line indicates the null difference. Magnitudes on the x axis are instrumental.

$H\alpha$ Survey (IPHAS; Drew et al. 2005) and the UV-Excess Survey (UVEX; Groot et al. 2009). We chose the IGAPS catalogue as a reference because, to our knowledge, it is the only one covering the M37 FOV in our three (u , g , i) filters, though its pass-bands are not exactly equal to ours. The IGAPS gri photometry is itself uniformly calibrated against the Pan-STARRS system (Chambers et al. 2016) with an internal accuracy of 0.02 mag (Monguió et al. 2020). The IGAPS U_{RGO} band is calibrated on a run-by-run basis across the M37 region.

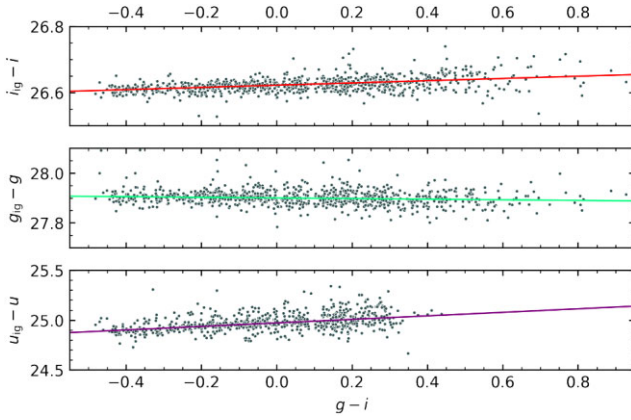


Figure 4. Calibration of the three filters (i , g , u): the coloured lines represent the linear fit.

We calibrated our photometry by using the relation $m_{\text{IGAPS}} - m_{\text{instr}}$ versus the colour index ($g - i$) in our instrumental magnitudes, as illustrated in Fig. 4. To obtain this relation we cross-matched our sources with the IGAPS catalogue. We considered the stars that were not saturated in both our exposures and IGAPS, and we linearly interpolated (for $m = i, g, u$) the $m_{\text{IGAPS}} - m_{\text{instr}}$ versus $g - i$ distribution. A first calibration has been performed using all the unsaturated stars in our catalogue, and after selecting the cluster members (see the next section), in order to mitigate potential systematic effects, we further restricted the sample to M37 members only. To transform the instrumental magnitudes we adopted the relation $m_{\text{cal}} = m_{\text{instr}} + a_0 + a_1 \times (g - i)$, where m_{cal} is our final magnitude calibrated with respect to IGAPS, and the coefficients are determined via a best-fitting approach. Higher order polynomials proved to be unnecessary.

4 SELECTION OF CLUSTER MEMBERS

The selection of member stars have been performed using the membership probabilities derived from Griggio & Bedin (2022). To select highly reliable cluster members we adopted the procedure that is displayed in Fig. 5. In the top left-hand panel, we show the membership probability plotted against the *Gaia*- G band magnitude. We applied a by-eye cut with the idea of selecting the bulk of sources with cluster membership at each magnitude. This cut is indicated by the dashed red curve, and we kept only the sources below that curve. This cut on the membership probabilities becomes less strict going towards fainter magnitudes as the measurement errors increase and members becomes less certain.

This sample has then been constrained on the parallax versus magnitude plane (top right-hand panel). We divided the data into magnitude bins of 1 mag, and for each bin we calculated $\sigma_{\varpi, i} = 68.27\text{th}$ percentile of the residuals around cluster's parallax ϖ (given by Griggio & Bedin 2022). We derived the red curves interpolating the points $\varpi \pm 2\sigma_{\varpi, i}$ with a spline.

The last selection was performed on the proper motions versus G plane. We applied the same procedure as for the parallax to μ_α and μ_δ to derive the red curves.

On the bottom right-hand panel, we show the spatial distribution of the stars that are selected as M37 members.

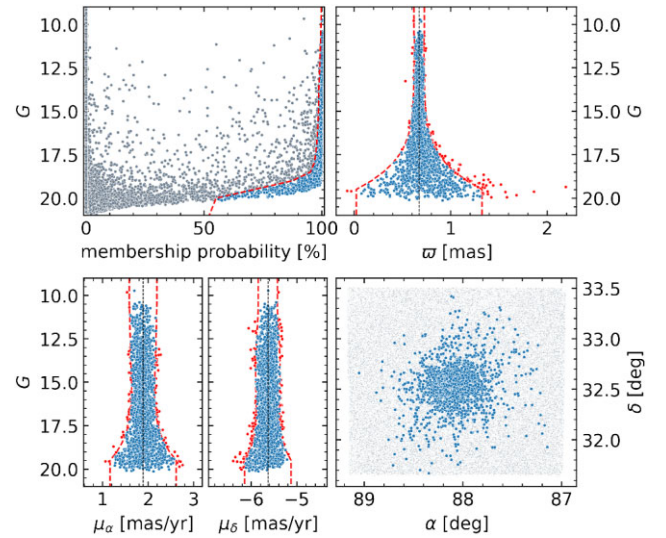


Figure 5. Members selection. Top left-hand panel: membership probability for all the sources. We reject the stars that fall above the red line. Top right-hand panel: G magnitude versus parallax. Here we reject the stars that fall outside the region delimited by the two red lines (blue dots). The black dashed line represents the median parallax. Bottom left-hand panel: proper motions of the sources that passed the previous two cuts versus their G magnitude. We kept the sources between the red dashed lines (blue dots). Bottom right-hand panel: spatial distribution of the sources. The blue dots are the selected members of M37.

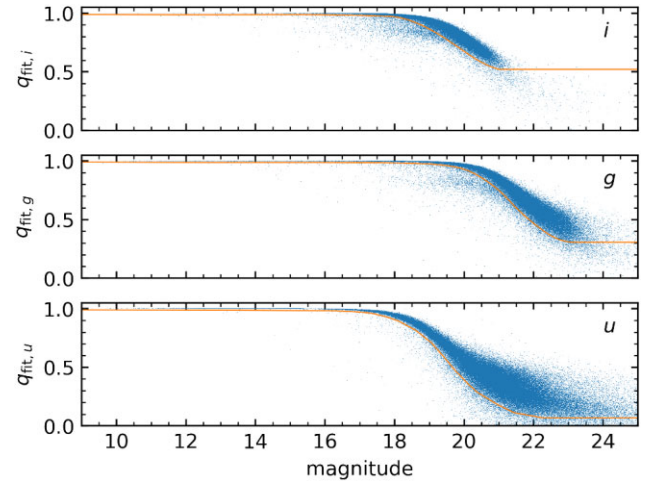


Figure 6. q_{fit} versus magnitude in each filter. We marked as good ($\text{pho_sel_f}=1$, $f = u, g, i$) the stars that are above the orange line and 3σ above the sky.

5 SLOAN COLOUR-MAGNITUDE DIAGRAMS

We first rejected sources with poor measurements, by applying a cut in the quality of fit (q_{fit}) parameter, which is in the KS2 output for each source. The q_{fit} measures how well a source is fitted by the PSF; a $q_{\text{fit}} = 1$ indicates a perfect fit. The cuts we performed are shown in Fig. 6. In addition to these cuts, we selected the sources that are at least 3σ above the sky background. The sources that passed these selection criteria and are not saturated are flagged with $\text{pho_sel_f} = 1$ in our catalogue, with $f = u, g, i$. The additional flag $\text{pho_sel} = 1$ is for stars that passed the selection in all the three filters.

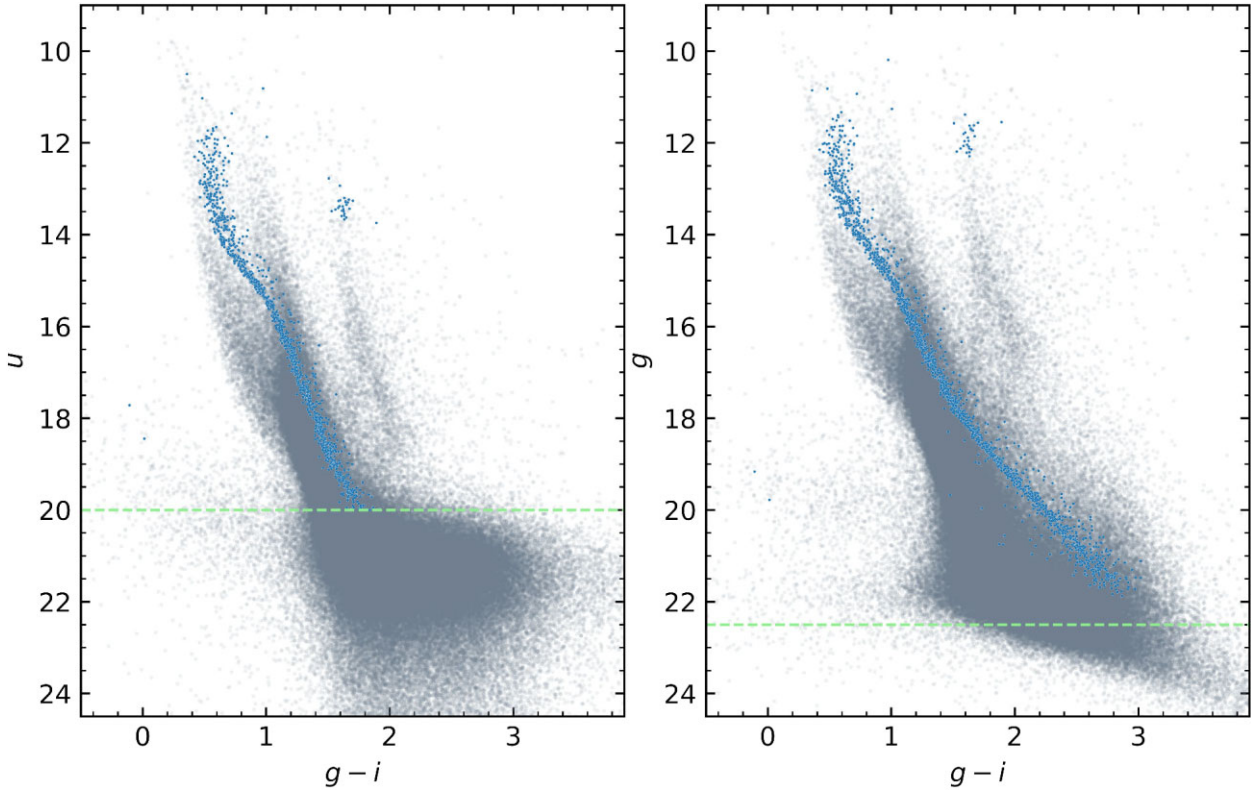


Figure 7. Colour–magnitude diagrams in *ugi* filters. The grey points represent the sources that passed the quality cuts in the considered filters of each CMD. The blue points are the sources that passed the members selection. The dashed green line represents the 3σ cut above the sky background level (in *u* and *g*, respectively).

In Fig. 7 we show a colour–magnitude diagram (CMD) of the selected sources in the FOV (in grey) of M37 and the cluster members as defined in previous section (in blue). The dashed green line represents the 3σ cut above the sky background in the *u* and *g* filters.

6 WHITE DWARF MEMBER CANDIDATES

M37 is known to host a few, faint white dwarf (WD) members, also including a very massive object of $\approx 1.3 M_{\odot}$ (Cummings et al. 2015, 2016). Given the current age of M37, the lightest WD members that could have formed through canonical single-star evolution are expected to have $\approx 0.7 M_{\odot}$. We focused our search for WD candidates at the hot-end of their cooling sequence that, however, for M37 corresponds to a region of the CMD where the measurement errors of *Gaia* are the largest.

We restricted our search to sources with $G_{BP} > 18$ and $-0.5 < G_{BP} - G_{RP} < 0.5$ where we expect to find WDs that have just recently formed and have both the same distance and reddening of M37 ($d = 1.5 \pm 0.1$ kpc, Griggio & Bedin 2022; $E(B - V) = 0.26$, Cordoni et al. 2018). We selected from this region the stars with proper motions and parallaxes that are compatible within 3σ with those of the cluster. To confirm the isolated WD nature of these objects we built a two-colour ($u - G_{BP}$, $g - G_{RP}$) diagram (Fig. 8), in which we identify the stars that passed this selection with an orange dot. Seven of them possess the typical blue colours of isolated WDs. All the previously known WD members of M37 are fainter than our *Gaia*-based selection (Cummings et al. 2015, 2016, and references therein).

The astrometric and photometric properties of the seven WD candidates are shown in Fig. 9 along with the other cluster members.

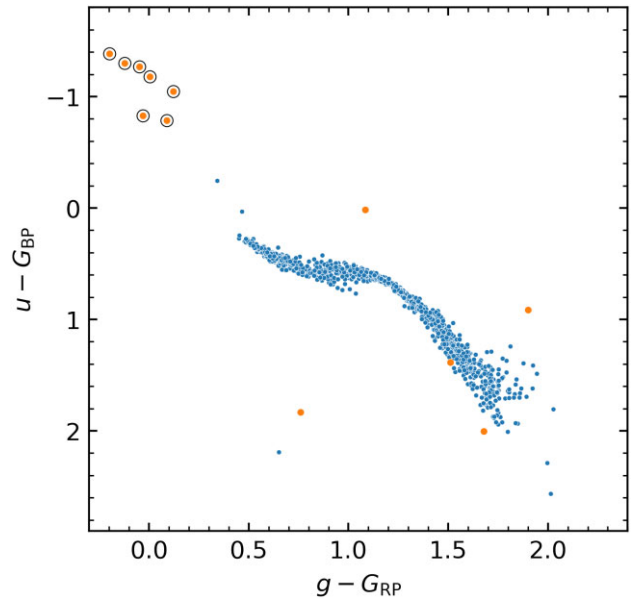


Figure 8. Two colour diagram of member stars. The blue points represent the cluster members. The orange dots indicate the sources that passed the selection described in the text. The orange dots encircled in black are those that we selected as WD member candidates.

Their relevant *Gaia* data are listed in Table 2. In Fig. A1 we show the finding charts for WD2–7, while that of WD1 is shown in Fig. 10 (right-hand panel).

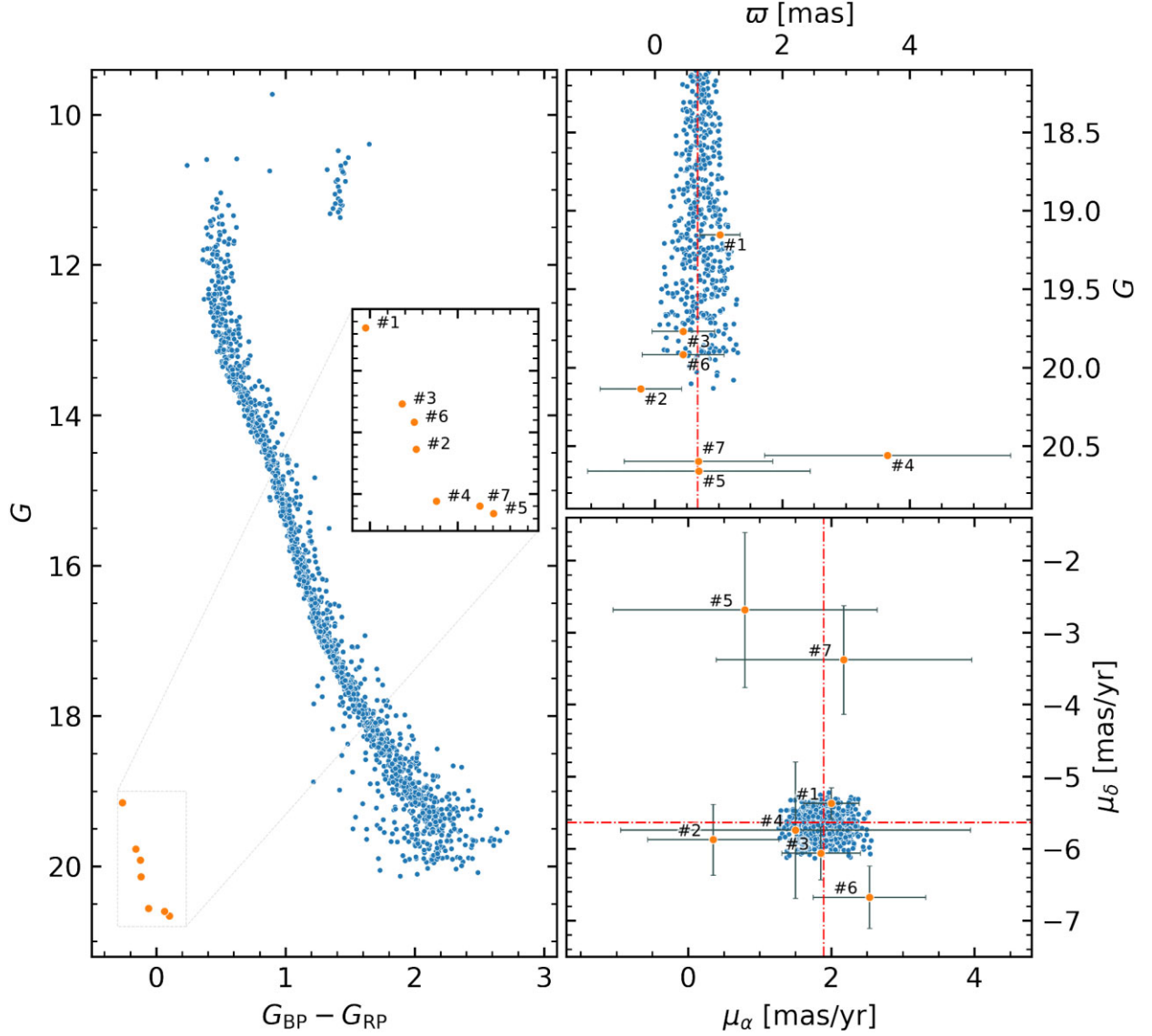


Figure 9. Left-hand panel: CMD of M37 members in the *Gaia* pass-bands (blue). The orange dots are the WD member candidates identified in this work. Error bars for parallax and proper motions are given by *Gaia* EDR3 uncertainties. Top right-hand panel: parallax versus *Gaia* G magnitude; the vertical red line represents the parallax of the cluster. Bottom right-hand panel: Proper motion diagram; the red lines represent the absolute proper motion of the cluster.

Table 2. Photometric and astrometric properties of the seven WD candidates.

#	<i>Gaia</i> EDR3 ID	G	G_{BP}	G_{RP}	g	u	i	μ_α (mas yr $^{-1}$)	μ_δ (mas yr $^{-1}$)	ϖ (mas)
WD1	3451205783698632704	19.154	19.100	19.362	19.164	17.716	19.271	2.003 ± 0.387	-5.371 ± 0.219	1.020 ± 0.315
WD2	3451182182857026048	20.137	20.038	20.156	20.160	18.859	19.923	0.353 ± 0.916	-5.877 ± 0.490	-0.224 ± 0.640
WD3	3451201076423973120	19.769	19.746	19.904	19.781	18.448	19.768	1.858 ± 0.550	-6.064 ± 0.368	0.444 ± 0.492
WD4	3451167786125150592	20.560	20.492	20.552	20.641	19.707	20.762	1.500 ± 2.443	-5.743 ± 0.946	3.649 ± 1.932
WD5	3451200114340263296	20.660	20.642	20.540	20.662	19.596	20.457	0.796 ± 1.845	-2.684 ± 1.076	0.688 ± 1.746
WD6	3448258267902375296	19.917	19.957	20.081	20.050	19.130	20.171	2.534 ± 0.787	-6.675 ± 0.435	0.443 ± 0.643
WD7	3454340495645123584	20.599	20.643	20.580	20.531	19.375	20.134	2.177 ± 1.786	-3.378 ± 0.755	0.682 ± 1.164

6.1 Spectroscopic follow-up of WD1

We collected optical spectra of the brightest candidate, WD1, with the Asiago Faint Object Spectrograph and Camera (AFOSC) mounted on the 1.82-m Copernico telescope operated by INAF-Osservatorio

Astronomico di Padova atop of Mount Ekar, Asiago, Italy. We used the gr4 grating with both 2.5 and 1.69-wide slits, achieving a resolving power of $R = 219$ and 325 at the central wavelength of gr4 for the two setups, respectively. One single exposure of 3600-s were taken on 2021 November 10, under hazy sky conditions

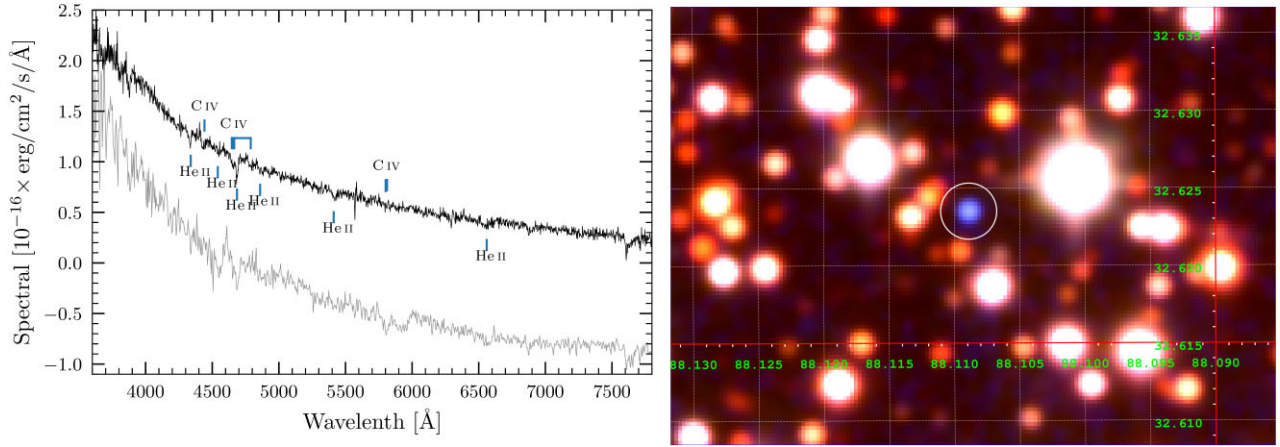


Figure 10. Left-hand panel: The TNG/LRS spectrum (black) and the Asiago/AFOSC spectrum (grey). The latter is shifted vertically by a constant factor. We have labelled some of the most prominent He II and C IV lines. Right-hand panel: Tri-chromatic stack finding-chart of WD1.

(slit 2.50 arcsec), while three exposures of 2700-s each were taken on 2022 January 12 under good sky conditions (slit 1.69 arcsec). The data were reduced with an IRAF (Tody 1986) based pipeline, i.e. FOSCGUI.² The average second-epoch spectrum signal-to-noise ratio (S/N) is around 15. A first look of the combined spectrum confirmed this star as a hot, likely hydrogen-deficient star.

We re-observed WD1 with the Device Optimized for the LOW RESolution (DOLORES, LRS in short) that is mounted on the Telescopio Nazionale Galileo (TNG) at the Observatorio del Roque de los Muchachos (Canary Islands, Spain). We took three exposures of 1800s each on 2022 March 3, in service mode during Director Discretionary Time (programme A44DDT3). We used the low-resolution blue grating (LR-B) with a 1-arcsec slit that enabled a dispersion of 2.8 Å pixel^{-1} and a resolution of 11 Å at 5577 Å . The observations were performed in dark time under good weather conditions and with a seeing well below 1 arcsec. The spectrophotometric standard Hiltner 600 was observed at the beginning of the night with the same slit width. The data were reduced, 1D optimally extracted and wavelength and flux calibrated by using standard reduction procedures with the STARLINK (Currie et al. 2014), PAMELA (Marsh 2014), and MOLLY (Marsh 2019) software packages. The average LRS spectrum of WD1 has $S/N = 35$ at 5500 Å . In Fig. 10, we show both the AFOSC and LRS spectra, labelling the most prominent absorption features of C IV at ≈ 4660 and $5801\text{--}5812 \text{ Å}$ and the He II lines.

6.2 Physical parameters

In order to shed more light on the properties of the seven WD candidates, we performed model fits of their Spectral Energy Distributions (SED). We collected available photometry from the *Galaxy Evolution Explorer* (GALEX DR6+7; Bianchi, Shiao & Thilker 2017), IGAPS (Monguió et al. 2020), PanSTARRS (Chambers et al. 2016), and the *Sloan* Digital Sky Survey (SDSS DR12; Alam et al. 2015). The SED fitting procedure allowed us to estimate the effective temperature

²FOSCGUI is a graphic user interface aimed at reducing spectrophotometric data and extracting spectroscopy of the focal reducer type spectrograph/camera FOSC. It was developed by E. Cappellaro. A package description can be found at <http://snrgroup.oapd.inaf.it/foscgui.html>.

Table 3. Physical parameters of six WD candidates obtained from the SED fitting analysis.

#	T_{eff} (K)	R/R_{\odot}	M/M_{\odot}	τ_{cool} (Myr)
WD2	46900^{+20900}_{-14700}	$0.019^{+0.005}_{-0.003}$	$0.52^{+0.11}_{-0.10}$	$1.9^{+2.2}_{-1.5}$
WD3	64500^{+10000}_{-11700}	$0.020^{+0.002}_{-0.002}$	$0.57^{+0.05}_{-0.05}$	$0.7^{+0.8}_{-0.4}$
WD4	60800^{+12100}_{-10800}	$0.015^{+0.001}_{-0.001}$	$0.67^{+0.08}_{-0.07}$	$0.8^{+1.0}_{-0.4}$
WD5	41900^{+16000}_{-9800}	$0.017^{+0.003}_{-0.002}$	$0.56^{+0.12}_{-0.09}$	$3.4^{+3.8}_{-2.5}$
WD6	35000^{+4200}_{-2700}	$0.024^{+0.002}_{-0.002}$	$0.44^{+0.03}_{-0.06}$	$3.1^{+1.6}_{-1.6}$
WD7	21100^{+2300}_{-2100}	$0.027^{+0.002}_{-0.002}$	$0.33^{+0.03}_{-0.04}$	$7.4^{+20.2}_{-5.6}$

(T_{eff}), radius, mass, and cooling age of the candidate WDs via χ^2 minimization of the difference among observed photometry and the appropriate synthetic magnitudes. The latter were computed from a grid of Koester (2010) models for hydrogen-dominated WD spectra (DA type), which we mapped on the La Plata cooling tracks (Althaus, Miller Bertolami & Corsico 2013; Camisassa et al. 2016). We adopted the distance of M37 and the differential reddening estimated (following the procedure described in Bellini et al. 2017b) from the cluster neighbours of each WD candidate as external priors in the SED fitting routine. The results of our SED fitting are shown in Fig. A2 for WD2–WD7. Their photometrically estimated physical parameters are listed in Table 3. The physical parameters of WD1 that could be obtained from the SED fitting routine would not be reliable, because this star is confirmed not to have a hydrogen-dominated atmosphere (see the next section). A spectroscopic follow-up of the most likely candidates (that is WD2, WD3, WD4, and WD5) remains necessary in order to independently confirm their cluster membership.

6.2.1 WD1

The LRS spectrum of WD1 confirms it as a hot, hydrogen-deficient WD that appears as an intermediate object between the PG 1159 and DO classes (Werner & Herwig 2006; Reindl et al. 2014). The spectral resolution and S/N of the spectra in hand are not sufficient for performing a quantitative spectral analysis, but its T_{eff} is likely hotter than $60\,000 \text{ K}$. This star was also identified by Frew (2017)

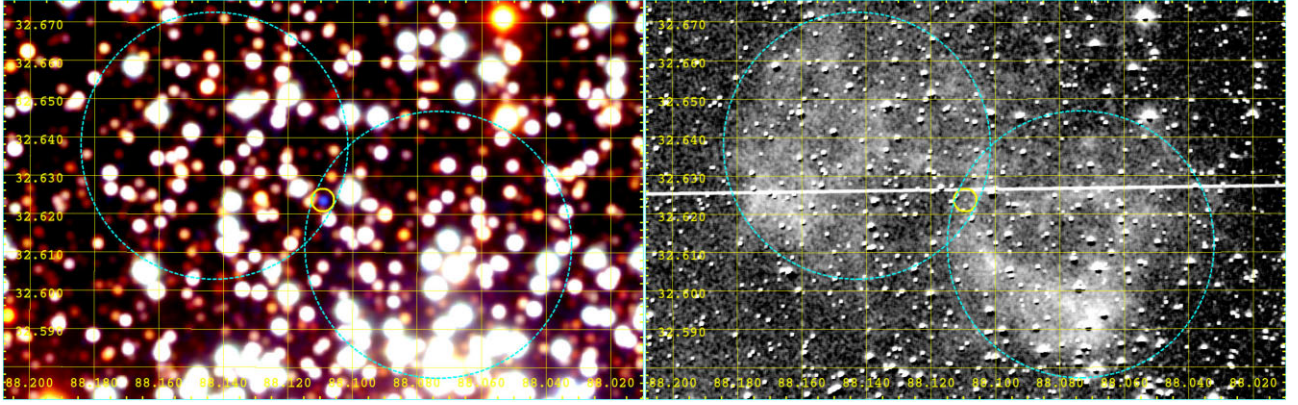


Figure 11. Left-hand panel: RGB stack of the region around WD1, encircled in yellow. The putative locations of the two lobes of the PN are encircled in cyan. Right-hand panel: $H\alpha-r$ image of the same region, which highlights the nebula, taken from the HASH data base (Parker, Bojićić & Frew 2016).

and Chornay & Walton (2021) as the central star of a faint, bipolar planetary nebula (PN) (PN G177.5+03.1; Parker et al. 2016). From Fig. 11 a diameter $d = 460$ arcsec can be estimated (consider $d = 4 \times r$, with r being the radius of one lobe). Assuming furthermore a distance of 1.5 kpc (Griggio & Bedin 2022), and an expansion velocity of 20 km s^{-1} , one can estimate the age of the PN to be 82 kyr. Such an old PNe can be expected for a star that has already entered the WD cooling sequence. The relation of this PN (shown in Fig. 11) with WD1 needs further confirmation: additional follow-up observations are needed to better characterize the evolutionary status and cluster membership of WD1 (that appears as a high-probability astrometric member of this cluster, having passed the membership selection criteria), via quantitative spectral analysis. If its physical properties and radial velocities turn out to be also compatible with the expected parameters (a mass that is larger than $0.7 M_{\odot}$, as well as a total age and mean radial velocity like those of the other M37 members) WD1 would represent a very rare (if not unique) central star of a planetary nebula (CSPN) that has passed all the tests of open cluster membership (Moni Bidin et al. 2014; Fragkou et al. 2019; Bond, Bellini & Sahu 2020).

6.2.2 WD2, WD3, and WD5

For these three stars we have estimated photometric masses that are within 2 or 3-sigmas from the minimum allowed mass for single star evolution of $0.7 M_{\odot}$. The estimated cooling ages are compatible with the total age of M37. In addition, WD3 passed the membership selection criteria.

6.2.3 WD4

This object is the most likely cluster member confirmed at the $1-\sigma$ level, as we obtain a $T_{\text{eff}} = 60\,800^{+12\,100}_{-10\,800}$ K, a mass of $0.67 \pm 0.08 M_{\odot}$, and a cooling age of $0.8^{+1.0}_{-0.4}$ Myr. If confirmed via spectroscopic follow-up, this WD could be one of the youngest evolved members of M37.

6.2.4 WD6 and WD7

Although they are likely very young, these two WD candidates have photometric estimates of radii and masses that are not compatible

with their proposed membership to M37. In fact, masses lower than $0.5 M_{\odot}$ are indicative of He-core WDs, originated from RGB stars with electron degenerate helium cores, that have lost their envelope before the onset of the helium flash. Given the age of this cluster, the presence of He-degenerate cores in the post-MS stars is very unlikely (theoretical isochrones predict post-MS stars with initial masses larger than $2.5 M_{\odot}$). Therefore, we do not believe that these two WDs can belong to M37.

7 A NEW CATALOGUE

With this paper, we publicly release a catalogue of the region described in Section 2. The catalogue contains photometry of 210 907 sources in the *Sloan*-like filters u , g , and i and *Gaia* EDR3 photometry and astrometry for the sources that are present also in the *Gaia* catalogue. The sources that are not detected by *Gaia* have the column `gid` set to zero. The value 999 is a placeholder for missing values (e.g. a source that has not been detected in the u filter has $u = 999$). The columns of the catalogue are described in Table A1. The catalogue and the stacked image are available at the following url: https://web.oapd.inaf.it/bedin/files/PAPERS_eMATERIALs/M37-ugiSchmidt/.

8 CONCLUSIONS

We reduced and analysed Schmidt images of the open cluster M37 combining our photometric catalogue with *Gaia* EDR3. We developed software tools to correct for the geometric distortion exploiting the *Gaia* reference system in the case of data from wide-field imagers collected with large-dithers. The set of routines that we developed for this specific instrument will be applied also to other wide-field imagers.

We have astrometrically and photometrically identified seven isolated WDs as candidate cluster members. We obtained follow-up low resolution spectra for one of them, confirming it as a hot, hydrogen-deficient (pre-) WD. This star was previously identified as the likely central star of a faint PN (Chornay & Walton 2020). Further follow-up spectroscopy is needed to univocally confirm it as one rare example of CSPN belonging to a Galactic open cluster. By means of spectral energy distribution analysis, we suggest that four out of seven WD candidates are likely or very likely cluster members. Follow-up spectroscopy is also needed to confirm their

cluster membership, eventually joining the already numerous family of degenerate stars found in this rich open cluster (Cummings et al. 2015, 2016).

We also publicly released a catalogue of 210 907 sources in a $\sim 2 \times 2 \text{ deg}^2$ region centred on M37, complementing the already existing data from IGAPS.

ACKNOWLEDGEMENTS

Based on observations collected at Schmidt and Copernicus telescopes (Asiago, Italy) of INAF. Partly based on observations collected with DOLORES@TNG under Director Discretionary Time program A44DDT3. This work has also made use of data from the European Space Agency (ESA) mission *Gaia* (<https://www.cosmos.esa.int/gaia>), processed by the *Gaia* Data Processing and Analysis Consortium (DPAC, <https://www.cosmos.esa.int/web/gaia/dpac/consortium>). Funding for the DPAC has been provided by national institutions, in particular the institutions participating in the *Gaia* Multilateral Agreement. MG, LRB, DN, LS, and AV acknowledge support by Ministero dell'Istruzione, dell'Università e della Ricerca under PRIN programme #2017Z2HSMF and by Istituto Nazionale di Astrofisica under PRIN-INAF 2019 programme #10-Bedin.

RR has received funding from the postdoctoral fellowship program Beatrui de Pinós, funded by the Secretary of Universities and Research (Government of Catalonia) and by the Horizon 2020 programme of research and innovation of the European Union under the Maria Skłodowska-Curie grant agreement No 801370. This research makes use of public auxiliary data provided by ESA/Gaia/DPAC/CU5 and prepared by Carine Babusiaux. This research used the facilities of the Italian Center for Astronomical Archive (IA2) operated by INAF at the Astronomical Observatory of Trieste. This research has made use of the HASH PN data base at hashpn.space.

DATA AVAILABILITY

All Schmidt data are publicly available at the INAF archive³ (P.I. Bedin). The *Gaia* EDR3 catalogue is accessible through the *Gaia* archive.⁴

REFERENCES

Alam S. et al., 2015, *ApJS*, 219, 12
 Althaus L. G., Miller Bertolami M. M., Córscico A. H., 2013, *A&A*, 557, A19
 Anderson J. et al., 2008a, *AJ*, 135, 2055
 Anderson J. et al., 2008b, *AJ*, 135, 2114
 Anderson J., Bedin L. R., Piotto G., Yadav R. S., Bellini A., 2006, *A&A*, 454, 1029
 Bedin L. R., Fontanive C., 2018, *MNRAS*, 481, 5339
 Bedin L. R., Salaris M., Piotto G., Anderson J., King I. R., Cassisi S., 2009, *ApJ*, 697, 965
 Bellini A., Anderson J., Bedin L. R., King I. R., van der Marel R. P., Piotto G., Cool A., 2017a, *ApJ*, 842, 6
 Bellini A., Anderson J., van der Marel R. P., King I. R., Piotto G., Bedin L. R., 2017b, *ApJ*, 842, 7
 Bianchi L., Shiao B., Thilker D., 2017, *ApJS*, 230, 24

Bond H. E., Bellini A., Sahu K. C., 2020, *AJ*, 159, 276
 Camisassa M. E., Córscico A. H., Althaus L. G., Shibahashi H., 2016, *A&A*, 595, A45
 Casamiquela L. et al., 2019, *MNRAS*, 490, 1821
 Catalán S., Isern J., García-Berro E., Ribas I., 2008, *MNRAS*, 387, 1693
 Chambers K. C. et al., 2016, preprint ([arXiv:1612.05560](https://arxiv.org/abs/1612.05560))
 Chornay N., Walton N. A., 2020, *A&A*, 638, A103
 Chornay N., Walton N. A., 2021, *A&A*, 656, A110
 Cordoni G., Milone A. P., Marino A. F., Di Criscienzo M., D'Antona F., Dotter A., Lagioia E. P., Tailo M., 2018, *ApJ*, 869, 139
 Cummings J. D., Kalirai J. S., Tremblay P. E., Ramirez-Ruiz E., 2015, *ApJ*, 807, 90
 Cummings J. D., Kalirai J. S., Tremblay P. E., Ramirez-Ruiz E., Bergeron P., 2016, *ApJ*, 820, L18
 Cummings J. D., Kalirai J. S., Tremblay P. E., Ramirez-Ruiz E., Choi J., 2018, *ApJ*, 866, 21
 Currie M. J., Berry D. S., Jenness T., Gibb A. G., Bell G. S., Draper P. W., 2014, in Manset N., Forshay P., eds, ASP Conf. Ser. Vol. 485, Astronomical Data Analysis Software and Systems XXIII. Astron. Soc. Pac., San Francisco, p. 391
 Drew J. E. et al., 2005, *MNRAS*, 362, 753
 Ferrario L., Wickramasinghe D., Liebert J., Williams K. A., 2005, *MNRAS*, 361, 1131
 Fragkou V., Parker Q. A., Zijlstra A. A., Crause L., Barker H., 2019, *Nat. Astron.*, 3, 851
 Frew D., 2017, Proc. IAU Symp., Vol. 323, Planetary Nebulae: Multi-Wavelength Probes of Stellar and Galactic Evolution. Cambridge Univ. Press, Cambridge, p. 11
 Gaia Collaboration, 2021, *A&A*, 649, A1
 Griggio M., Bedin L. R., 2022, *MNRAS*, 511, 4702
 Groot P. J. et al., 2009, *MNRAS*, 399, 323
 Heiter U., Soubiran C., Netopil M., Paunzen E., 2014, *A&A*, 561, A93
 Kalirai J. S., Richer H. B., Reitzel D., Hansen B. M. S., Rich R. M., Fahlman G. G., Gibson B. K., von Hippel T., 2005, *ApJ*, 618, L123
 Kalirai J. S., Ventura P., Richer H. B., Fahlman G. G., Durrell P. R., D'Antona F., Marconi G., 2001, *AJ*, 122, 3239
 Kang Y. B., Kim S.-L., Rey S.-C., Lee C.-U., Kim Y. H., Koo J.-R., Jeon Y.-B., 2007, *PASP*, 119, 239
 Kharchenko N. V., Piskunov A. E., Röser S., Schilbach E., Scholz R. D., 2005, *A&A*, 438, 1163
 Koester D., 2010, Mem. Soc. Astron. Italiana, 81, 921
 Libralato M. et al., 2015, *MNRAS*, 450, 1664
 Marsh T. R., 2014, PAMELA: Optimal Extraction Code for Long-Slit CCD Spectroscopy, record ascl:1406.002
 Marsh T., 2019, molly: 1D Astronomical Spectra Analyzer, record ascl:1907.012
 Mermilliod J.-C., Huestamendia G., Del Rio G., Mayor M., 1996, *A&A*, 307, 80
 Monguió M. et al., 2020, *A&A*, 638, A18
 Moni Bidin C. et al., 2014, *A&A*, 561, A119
 Nardiello D. et al., 2018, *MNRAS*, 481, 3382
 Netopil M., Paunzen E., Heiter U., Soubiran C., 2016, *A&A*, 585, A150
 Pancino E., Carrera R., Rossetti E., Gallart C., 2010, *A&A*, 511, A56
 Parker Q. A., Bojčić I. S., Frew D. J., 2016, *J. Phys. Conf. Ser.*, 728, 032008
 Piskunov A. E., Schilbach E., Kharchenko N. V., Röser S., Scholz R. D., 2008, *A&A*, 477, 165
 Reindl N., Rauch T., Werner K., Kepler S. O., Gänsicke B. T., Gentile Fusillo N. P., 2014, *A&A*, 572, A117
 Richer H. B. et al., 2021, *ApJ*, 912, 165
 Salaris M., Serenelli A., Weiss A., Miller Bertolami M., 2009, *ApJ*, 692, 1013
 Sarajedini A., Brandt K., Grocholski A. J., Tiede G. P., 2004, *AJ*, 127, 991
 Scalco M. et al., 2021, *MNRAS*, 505, 3549
 Tody D., 1986, in Crawford D. L., ed., Proc. SPIE Conf. Ser. Vol. 627, Instrumentation in Astronomy VI. SPIE, Bellingham, p. 733
 Werner K., Herwig F., 2006, *PASP*, 118, 183

³<http://archives.ia2.inaf.it/aa/>

⁴<https://gea.esac.esa.int/archive/>

SUPPORTING INFORMATION

Supplementary data are available at [MNRAS](https://www.mnras.org/) online.

CATALOG.zip

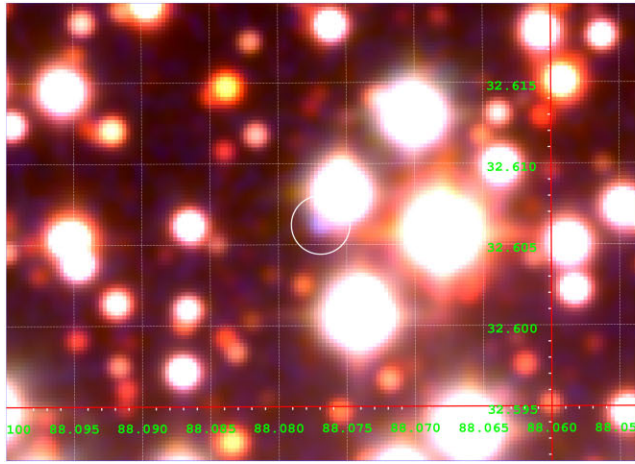
Please note: Oxford University Press is not responsible for the content or functionality of any supporting materials supplied by the authors. Any queries (other than missing material) should be directed to the corresponding author for the article.

APPENDIX: ADDITIONAL FIGURES

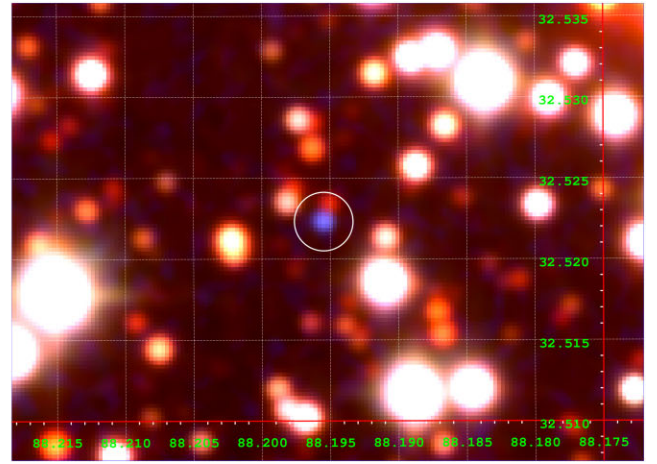
In this section we give a description of the catalogue's columns in Table A1, and we show the finding charts and the best fit results for the SED analysis of six WD candidates in Figs A1 and A2.

Table A1. Description of the columns in our catalogue.

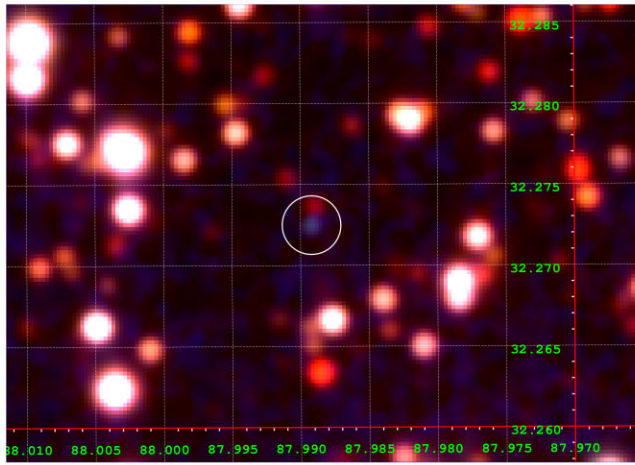
Column	Description
gid	<i>Gaia</i> EDR3 id of the source
ra	right ascension (deg)
dec	declination (deg)
i	magnitude in the <i>i</i> filter
ei	error on the <i>i</i> mag
g	magnitude in the <i>g</i> filter
eg	error on the <i>g</i> mag
u	magnitude in the <i>u</i> filter
eu	error on the <i>u</i> mag
qi	quality flag for <i>i</i> mag
qg	quality flag for <i>g</i> mag
qu	quality flag for <i>u</i> mag
oi	fraction of flux within the PSF aperture in <i>i</i> filter due to neighbours
og	fraction of flux within the PSF aperture in <i>g</i> filter due to neighbours
ou	fraction of flux within the PSF aperture in <i>u</i> filter due to neighbours
pho_sel	1 if source passed photometric cuts in all filters
pho_sel_i	1 if source passed photometric cuts in the <i>i</i> filter
pho_sel_g	1 if source passed photometric cuts in the <i>g</i> filter
pho_sel_u	1 if source passed photometric cuts in the <i>u</i> filter
G	magnitude in the <i>Gaia</i> EDR3 <i>G</i> filter
eG	error on the <i>G</i> mag
Gbp	magnitude in the <i>Gaia</i> EDR3 <i>G_{BP}</i> filter
eGbp	error on the <i>G_{BP}</i> mag
Grp	magnitude in the <i>Gaia</i> EDR3 <i>G_{RP}</i> filter
eGrp	error on the <i>G_{RP}</i> mag
PI	parallax (mas)
ePI	error on parallax (mas)
muRa	proper motion on ra (mas yr ⁻¹)
emuRa	error on muRa (mas yr ⁻¹)
muDec	proper motion on dec (mas yr ⁻¹)
emuDec	error on muDec (mas yr ⁻¹)
P	membership probability
member	1 for sources that passed our members selection



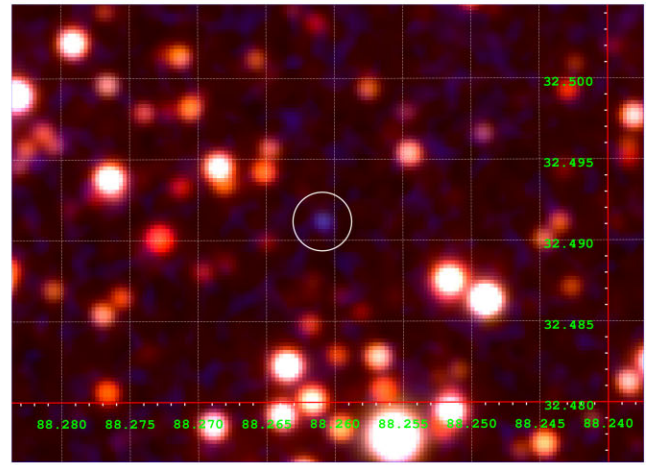
(a) WD2



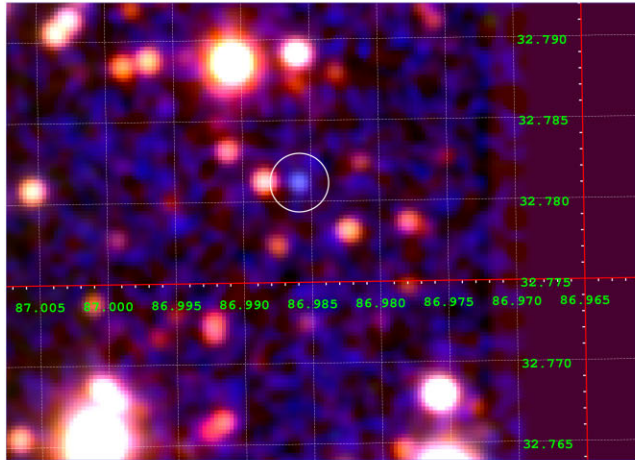
(b) WD3



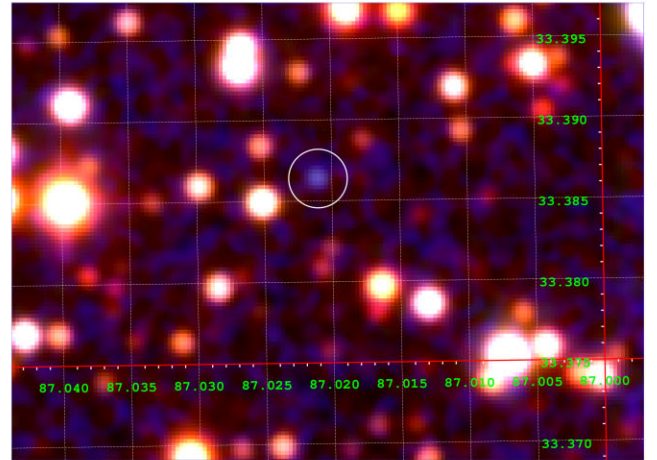
(c) WD4



(d) WD5



(e) WD6



(f) WD7

Figure A1. Finding charts of six WD candidates.

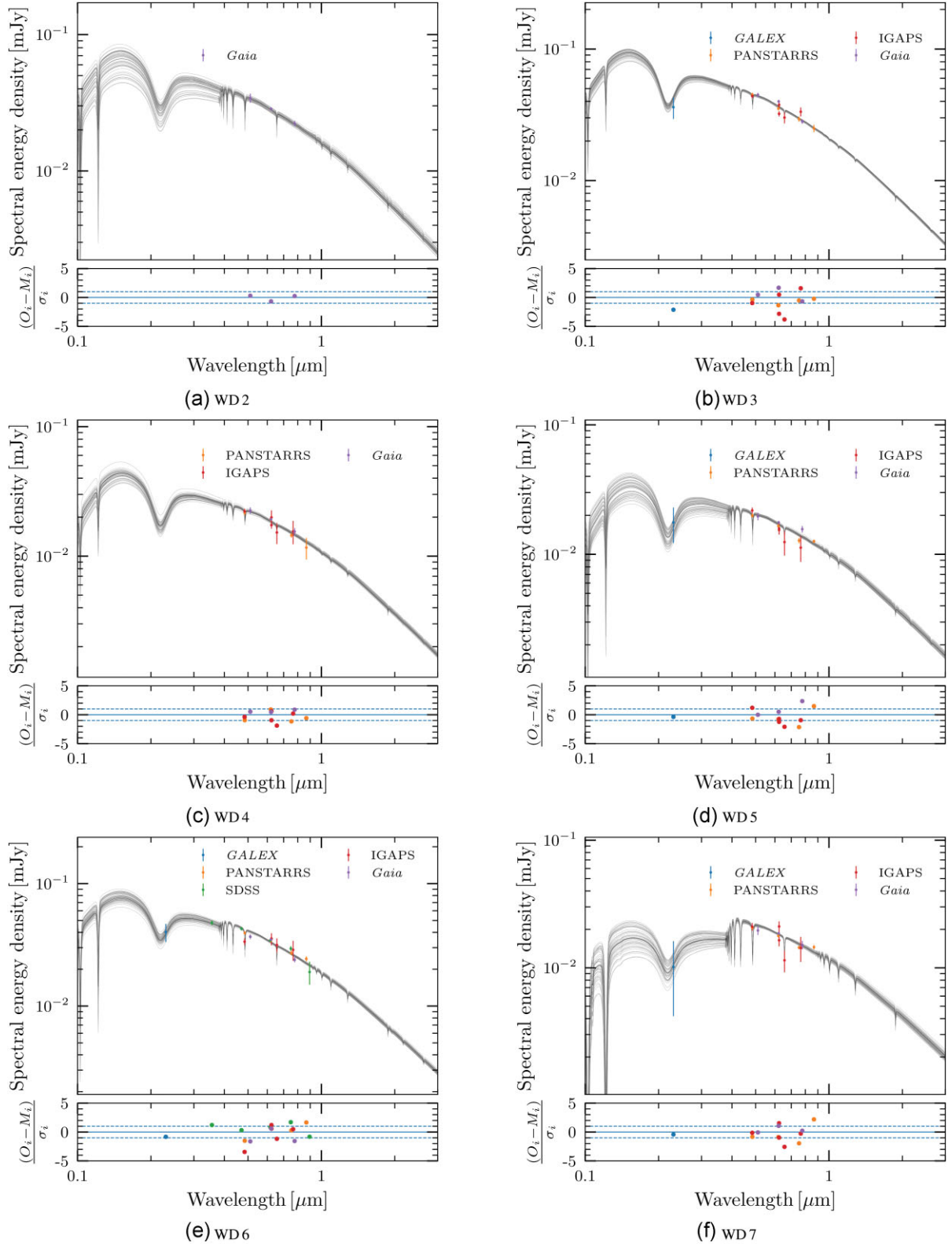


Figure A2. Best-fitting results for the SED analysis of six WD candidates. In each panel, the upper plot shows the best-fitting model (black) and the models corresponding to the uncertainty range (grey). The bottom plots represent the residuals among the used photometry and the best-fitting model.

This paper has been typeset from a \LaTeX file prepared by the author.